HHS Public Access

Author manuscript

Biomaterials. Author manuscript; available in PMC 2018 May 01.

Published in final edited form as:

Biomaterials. 2017 May ; 127: 25–35. doi:10.1016/j.biomaterials.2017.02.037.

Active targeting theranostic iron oxide nanoparticles for MRI and magnetic resonance-guided focused ultrasound ablation of lung cancer

Zhongling Wang[a,e], **Ruirui Qiao**[b], **Na Tang**[a], **Ziwei Lu**[c], **Han Wang**[a], **Zaixian Zhang**[d], **Xiangdong Xue**[e], **Zhongyi Huang**[e], **Siruo Zhang**[e], **Guixiang zhang**[a,**], and **Yuanpei Li**[e,*]

[a]Department of Radiology, Shanghai General Hospital of Nanjing Medical University, Shanghai 200080, China

[b]1.Institute of Chemistry, Chinese Academy of Sciences, BeiYiJie. 2.Zhong Guan Cun, Beijing 100190, China, University of Chinese Academy of Sciences, Beijing 100049, China

[c]Department of Radiology, The First Affiliated Hospital of Soochow University, Suzhou, Jiangsu 215006, China

[d]Radiology Department, the affiliated Hospital of Qingdao University, Qingdao, Shandong 266003, China

[e]Department of Biochemistry & Molecular Medcine, UC Davis Comprehensive Cancer Center, University of California, Davis, Sacramento, CA 95817, USA

Introduction

Magnetic resonance-guided focused ultrasound surgery (MRgFUS), as a promising non-invasive ultrasound thermal treatment for soft tissue lesions, has been utilized in the treatment of prostate, kidney, and liver cancer [1–3]. In particular, there is precise control of beam direction and ongoing feedback is provided to detail temperature changes at and around the treated tissue in MRgFUS. The main advantages of MRgFUS are that it is non-invasive, able to provide real-time, three-dimensional imaging, and closed-loop MR feedback. Magnetic resonance imaging (MRI) is a clinically useful diagnostic and tumor detection technique and can provide real-time temperature monitoring in MRgFUS. MRgFUS ablation usually involves the use of gradient-echo MR imaging for real-time temperature monitoring, based on spin-lattice (T_1) relaxation time and temperature sensitivity of the proton resonance frequency [4]. The tumor ablation efficiency of MRgFUS highly depends on its capacity to deposit energy in tissue. However, when shifting from an *in vitro* environment to *in vivo* tissue, there is considerable attenuation of ultrasonic energy emitted by the MR-guided ultrasound transducer [5]. High ultrasound power must be employed to improve the therapeutic efficiency and guidance of conventional MRgFUS in

**Corresponding author: Guixiang Zhang, guixiangzhang002@163.com. *Corresponding author: Yuanpei Li, lypli@ucdavis.edu.

order to achieve reduction effects on a deeper lesion. This high ultrasound power could cause severe side effects, such as skin burns, edema, perforation of intestines, and injury of peripheral nerve surrounding the tumor [6]. Furthermore, the set current is not sensitive enough to visualize small lesions using conventional MRgFUS settings [6–9].

Due to their excellent biocompatibility and magnetic properties, superparamagnetic iron oxide (SPIO) NPs have been used extensively for drug delivery, MRI probes, and tumor thermotherapy [7–14]. Previous studies have shown that dipole relaxation induced by an alternating magnetic field can contribute to magnetic hyperthermia of SPIO NPs. During irradiations of near-infrared (NIR) laser light and high intensity focused ultrasound (HIFU) treatment, SPIO NPs were used to induce the thermal therapy effect in tumor tissue [6, 15–19]. Recently, superparamagnetic iron oxide-polymer composite microcapsules (mean diameter, 587 nm & 885.6 nm) have been proposed for MRgFUS [5, 17]. These microcapsules were demonstrated with the ability to enhance ultrasonic wave absorption and energy deposition in the targeted tissue, thereby enhancing the tumor-ablative effects of MRgFUS [17]

In the present study, we propose to develop an active targeting, nanosized theranostic SPIO nanoplatform to improve the MRI sensitivity and tumor-ablative efficacy of a clinical MRgFUS system. These SPIO nanoparticles were coated with a layer of polyethylene glycol (PEG) to improve their biocompatibility [14, 20]. Epidermal growth factor receptor (EGFR) is a tyrosine kinase cellular transmembrane receptor and is linked to aberrant survival and poor prognosis. It is overexpressed in various epithelial tumors, such as non-small cell lung, kidney, breast, and head-and-neck squamous cell carcinoma [21, 22]. In this study, the surface of these PEGylated SPIO nanoparticles was further decorated with high affinity anti-EGFR monoclonal antibody (Cetuximab) to form a nanocomposite (anti-EGFR-PEG-SPIO) for targeted delivery to EGFR overexpressing H460 lung cancer. The anti-EGFR-PEG-SPIO was physicochemically characterized. Their targeting capability, MRI contrast enhancement and cytotoxicity were studied in H460 lung cancer cells as well as in nude rat models bearing H460 lung cancer xenografts. The capability of anti-EGFR-PEG-SPIO for synergistic MRgFUS treatment of cancer and the applications of a series of MRI approaches for non-invasive monitoring treatment response were demonstrated using nude rat lung tumor models (Scheme shown in Fig. 1a). To the best of our knowledge, this study represents the first evaluation of an active targeting and nano-sized SPIO platform for the enhancement of imaging sensitivity and tumor-ablative efficacy in MRgFUS.

2 Materials and method

2.1 Preparation of Fe_3O_4 nanoparticles

Iron oxide nanoparticles were produced according to a reported procedure[23, 24]. In brief, $Fe(acac)_3$ (2.12 g, 6 mmol), HOOC-PEG-COOH (0.12 M, M.W.=2000), and oleylamine (7.90 mL, 24 mmol) were mixed in 100 mL of diphenyl oxide solution. The above solution was heated to reflux under a nitrogen environment. Next, the iron solution was stirred at 400 rpm. In order to monitor the particle growth and formation, different aliquots were extracted during the heating process. Upon addition of a mixture of ethanol and ether (vol:vol = 1:5) into the aliquots at 37 °C, the reaction mixture was deposited and isolated. After the wash,

the deposit was dissolved in ethanol. Subsequently, the solution was precipitated with ether for three cycles. Finally, the nanoparticles were purified and collected for further use.

Anti-EGFR-PEG-SPIO was synthesized based on a previously published method[20, 23]. Briefly, PEGylated SPIO (Fe 2 mg, 3.5 mg/mL) was added into a 2 mL Eppendorf tube. 1-ethyl-3-(3-dimethylaminopropyl carbodiimide) (EDC) and *N*-hydroxysulfosuccinimide sodium salt (sulfo-NHS) were dissolved in PBS buffer and quickly transferred to the PEGylated SPIO solution. Then, the mixture was allowed to react for 15 min at room temperature. Afterwards, the solution was purified by a PD-10 column with $NaHCO_3$/Na_2CO_3 buffer (pH=8.5). Cetuximab (1 mg) was added into the purified PEGylated SPIO solution, and the reaction was stored at 4 °C overnight. Anti-EGFR-PEG-SPIO was obtained after the buffer was transferred to PBS by an ultracentrifugation process.

2.2 Characterization of Anti-EGFR-PEG-SPIO

The morphology of these nanoparticles was observed by transmission electron microscopy (TEM, FEI Tecnai G20). The hydrodynamic diameter of these nanoparticles before and after conjugation with anti-EGFR mAb was performed by dynamic light scattering (DLS, Nano ZS, Malvern) at room temperature. Hysteresis loop was investigated by a Quantum Design MPMS 5MPMS superconducting quantum interference device magnetometer at room temperature. Regaku D/Max-2500 diffractometer was employed to record X-ray diffraction (XRD) pattern and structural properties of the nanoparticle samples. The T_2 values of the anti-EGFR-PEG-SPIO and PEGylated SPIO nanoparticles were carried out at 3.0 T MRI Scanner (GE signa HDx, USA.) at 37 °C. The acquisition parameters were: TR=4000 ms, TE=60 ms; slice thickness=1 mm; slice spacing=1 mm. A 64 mm square field of view (FOV) was used with an image matrix of 256 × 256. The relativities r_2 ($mM^{-1}s^{-1}$) were calculated from the fitting of the $1/T_2$ versus plots.

2.3 Cell culture and animal models

NCI-H460 was obtained from the Academy of Life Sciences (Shanghai, China). RPMI 1640 medium, fetal bovine serum (FBS), streptomycin, and penicillin were obtained from Jinuo Biomedical Technology Co. Ltd. (HangZhou, China). H460 cells were cultured at 37 °C in RPMI 1640 medium containing fetal bovine serum (10%), streptomycin, and penicillin in a humidified atmosphere with 5% CO_2.

Nude rats, 4 weeks of age, were obtained from Charles River Laboratory Animal Technology Co. Ltd. (Beijing, China). All animal experiments were performed under the requirements of the Use and Care of Animals Committee at Nanjing Medical University, Shanghai General Hospital according to institutional guidelines. H460 cells in a 200 uL mixture of PBS suspension were injected into the left posterior thigh muscles of nude rats. The tumor sizes for all nude rats were monitored and recorded weekly. Tumors reaching a longest dimension of 1.0 cm were used for *in vivo* MR imaging and MRgFUS ablation.

2.4 In vitro cytotoxicity

The cytotoxicity of anti-EGFR-PEG-SPIO and PEGylated SPIO was analyzed by MTT (methyl thiazolyl tetrazolium) assay on H460 cells according to a standardized method [25].

A density of 3×10^5 H460 cells were seeded in 96-well plates and then incubated for 24 h (37 °C, 5% CO_2) in RPMI 1640 medium. H460 cells were incubated for 24 h with media containing anti-EGFR-PEG-SPIO and PEGylated SPIO at different iron concentrations (5, 10, 20, 40, 60, 80 μg/mL). Post incubation, 50 μL of MTT stock solution (5 mg/mL) was added to each well. After 4 h, the media was aspirated and 150 μL dimethyl sulfoxide (DMSO) was added to dissolve the crystal. Absorbance was measured at 490 nm using a microplate reader to assess cell viability.

2.5 Prussian blue staining and TEM

H460 cells were seeded into a 96-well plate at a density of 4×10^5 cells per well and was incubated with anti-EGFR-PEG-SPIO and PEGylated SPIO in iron concentrations of 40 μg/mL for 1 h. Then, the cells were washed and fixed with 4% glutaraldehyde for 20 min, and stained with Prussian blue according to a previous reported study [25].

The cellular uptake of anti-EGFR-PEG-SPIO and PEGylated SPIO was further evaluated by TEM imaging (Hitachi, Japan) with an operating voltage of 60 KV [25, 26]. In brief, the cells were seeded at a density of 4×10^5 cells per well into a six-well plate for 24 h, reaching a confluency of 80%, and then treated with PEGylated SPIO and anti-EGFR-PEG-SPIO for 12 h at room temperature. The embedded cells were sectioned (75 nm) and mounted onto 200-mesh copper grids after washing with phosphate buffer.

2.6 In vitro MRI on H460 tumor cells

An *in vitro* MRI was performed on H460 cells (1×10^6) that were incubated with anti-EGFR-PEG-SPIO and PEGylated SPIO for 2 h. After incubation with different Fe concentrations (0–80 μg/mL), cells were digested with 0.25% trypsin, centrifuged for 3 min, and resuspended in agarose (1 mL, 0.5 %) using an Eppendorf tube. MR imaging was obtained in a 3.0 T MR system. T_2WI images were performed using the following parameters: TR/TE=3000 ms/90.4 ms; slice thickness=1 mm; slice spacing=1 mm; matrix=256 × 256; FOV=8 cm × 8 cm. The T_2 signal intensities were measured within the region of interest (ROI).

2.7 In vivo MR imaging of H460 tumor

Nude rats bearing H460 lung cancer were scanned on a 3.0 T MR system with a high resolution animal coil at 0.5, 1.0, 2.0, 4.0, 6.0, 10, and 12 h after injection of the anti-EGFR-PEG-SPIO (n=6) and PEGylated SPIO agents (n=6) (1 mL, 40 μg/mL) via tail vein. All rats were imaged under the T_2W spin-echo sequence (TR/TE=4000/96.7 ms) with a 256 × 256 matrix size. The mean T_2-weighted signal intensities were measured for each tumor (Smean). Then, the relative signal-to-noise ratio (SNR = Smean/NSD (standard deviation of the background signal)) was calculated based on a previously reported method [25].

2.8 Biodistribution of targeting and nontargeting NPs

Nude rats were sacrificed at 12 h post MR scanning. Liver, spleen, heart, lung, stomach, intestines, kidneys, blood, and tumor tissues were collected and weighed. The iron concentration in the samples was measured with inductively coupled plasma atomic

emission spectroscopy (ICP-AES, Leeman Prodigy, USA). Nude rats bearing H460 lung cancer xenografts injected with PBS were used as a control group.

2.9 MR guided FUS System

All animal experiments were performed on the FUS system (Insightic, Inc., Haifa, Israel) and on a 3.0 T MR Signa HDxt system. Nude rats were anesthetized with 1 mL of 3% sodium pentobarbital by intraperitoneal injection, and were then randomly divided into positive control group (n=6), negative control group (low power, n=6), PEGylated SPIO group (n=6), and anti-EGFR-PEG-SPIO group (n=6). The nude rats tumors were sonicated after injection of the PEGylated SPIO and anti-EGFR-PEG-SPIO solution (1 mL, 40 μg/mL) via tail vein at 4.0 h. Prior to sonication, T_2-weighted spin-echo sequence were acquired (TR/TE=4000/96.7 ms; slice thickness, 3 mm; matrix, 320 × 256; FOV, 8 cm × 8 cm). For each nude rat, two to five sonications were planned. A single-point pulsed sonication (Acourstic energy 30–80 W, spot energy 600–1400 J, frequency 1.0–1.2 MHz, sonication duration 25 s) was delivered to produce mechanical force in the tumor region. The treated areas were about 0.5 cm^2 according to the pretreatment plan. Each dynamic temperature was monitored by real-time MRI temperature mapping of the treated area. The temperature of the treated tumor was increased to 65–80 °C.

2.10 Post thermal therapy MR imaging

Following thermal therapy, MR images were acquired to observe the tumor treatment effect. Post-thermal therapy MR images were performed at 0.5 h, 3, 7, 14 and 30 d. The dynamic T_1-weighted images (TR/TE=560 ms/15 ms; slice thickness, 2 mm; matrix, 320 × 256; FOV, 8 cm × 8 cm) were obtained in the axial and sagittal planes. Gadolinium diethylene-trianmine pentaacetic acid (Gd-DTPA) (0.2 mL/kg) was administered through injection of tail vein. Fast spin-echo T_2-weighted images were obtained using same parameters. For DWI, a single shot echoplanar pulse sequence (TR/TE=1924/60 ms), T_2 signal intensity, apparent diffusion coefficient (ADC) values, and tumor size were measured. All nude rats in four groups were sacrificed, and the tumors were harvested for histopathology evaluation.

2.11 Statistical analysis

All data analyses were presented as mean ± standard deviation (SD). Analysis was carried out using SPSS 19.0 software. MRI signal intensity was compared using univariate Analysis of Variance, and we used SNK test for binary comparison. All statistical significance was assigned a p value less than 0.05.

3. Results and discussion

3.1 Synthesis and characterization of anti-EGFR-PEG-SPIO

We were able to successfully synthesize anti-EGFR-PEG-SPIO, and utilize TEM, DLS, XRD, and hysteresis loop to characterize their size, composition and magnetic properties. TEM image of PEGylated SPIO before ligand decoration showed a uniform size distribution with a mean diameter of about 9.2 nm (Fig. S1a). DLS results demonstrated that the hydrodynamic diameter was about 38.5 nm for PEGyloated SPIO and 45.7 nm for EGFR-targeted NPs, respectively (Fig. 1b). Based on the XRD results, we calculated the SPIO size

by Scherrer equation [27]. The XRD calculated size was 8.73 nm, which was in line with the TEM results (9.2 nm) showed in Fig. S1a. The anti-EGFR-PEG-SPIO and PEGylated SPIO exhibited a typical superparamagnetic behaviour with a magnetization (M) value of 58 emu/g and 60 emu/g (Fig. 1c). The T_2 values of the anti-EGFR-PEG-SPIO and PEGylated SPIO were 10.3 and 11.2 ms, respectively, while the T_2 relativity values were 97.1 $s^{-1}mM^{-1}$ and 89.3 $s^{-1}mM^{-1}$, respectively, when measured on a 3.0 T MRI Scanner (Fig. 1d). The XRD result indicated that characteristic peaks of NPs were not changed after modification with PEG-SPIO (Fig. S1b). The above result confirmed that the EGFR antibody was conjugated successfully on the surface of PEGylated SPIO. The anti-EGFR-PEG-SPIO NPs dissolved in water or PBS remained stable for 3 months at 4 °C, indicating their great stability and water solubility.

3.2 Cytotoxicity assay of anti-EGFR-PEG-SPIO NPs and PEGylated SPIO in H460 cells

The cytotoxicity of the anti-EGFR-PEG-SPIO and PEGylated SPIO in H460 cells was evaluated by MTT assay before administrating the nanoparticles for *in vivo* application. Cell viability with these nanoparticles at different iron concentrations (5, 10, 20, 40, 60, 80 μg/mL) was measured after 24 h of incubation (Fig. 2). The MTT result showed that the viability of H460 cells was above 96% at 5 μg/mL, and dropped to 85% when 80 μg/mL was present. These results demonstrated no obvious cytotoxicity for both anti-EGFR-PEG-SPIO and PEGylated SPIO at tested concentrations in H460 cells.

3.3 In Vitro Cellular Uptake

The uptake of anti-EGFR-PEG-NPs and PEGylated NPs in the H460 cell line was determined by Prussian blue staining (Fig. 3a and b). The H460 cells treated with anti-EGFR targeting NPs showed more blue appearance than non-targeting NPs at the same iron concentration (40 μg/mL). This result indicated that EGFR receptor-mediated endocytosis could increase the uptake rate of PEGylated SPIO. TEM was utilized to further investigate the subcellular distributions of the two types of nanoparticles (anti-EGFR targeting vs non-targeting NPs). Numerous electron staining particles could be observed in the cell endosome after treatment with anti-EGFR-PEG-SPIO NPs for 12 h (Fig. 3c and d). In contrast, H460 cells incubated with non-targeting PEGylated SPIO did not show obvious electron-dense particles in TEM. Our results suggested that the increased cellular uptake of anti-EGFR targeted NPs may be due to the EGFR receptor-mediated endocytosis pathway.

3.4 Targeted MR imaging in vitro

To further investigate the *in vitro* EGFR targeting of anti-EGFR-PEG-SPIO on H460 cells, we measured the T_2 weighted signal intensity of H460 cells after incubation with different iron concentration of NPs. As the iron concentration in EGFR targeting NPs group increased, the T_2 signal intensity decreased significantly. The rate of signal intensity change was −58.2%, −82.7%, −94.4%, and 98.3% respectively, at the iron concentrations of (10, 20, 40, 80 μg/mL). MRI signal intensity of H460 cells with EGFR overexpression treated with anti-EGFR-PEG-SPIO decreased more significantly than the group treated with PEGylated SPIO ($P<0.01$) (Fig. 4a and b, and Tab. S1). This was in consistency with the above Prussian blue staining and TEM results, and further demonstrated that the anti-EGFR mAb was able to increase the cellular uptake of NPs via binding with EGFR on the surface of H460 cells.

The increased uptake of SPIO nanoparticles in cells decreased their T_2 signal intensity values in MRI. Collectively, the results indicated that the effect of active targeting via anti-EGFR in EGFR overexpressed cells could be achieved by anti-EGFR-PEG-SPIO in H460 cells *in vitro* and this targeted delivery process could be monitored by MRI. It has been reported that the protein corona could establish a barrier and screen the interactions between the ligand and its target on a separate surface, and therefore significantly reduce NP targeting efficiency[28, 29]. We also considered this issue in our work. The SPIO nanoparticles used in the present work were based on our previous study [30], in which we incubated the SPIO nanoparticles with BSA and IgG (major proteins in serum), and investigated the interactions between the nanoparticles and proteins. The results supported that oleylamine and PEG co-stabilized SPIO nanoparticles (used in this work) enabled to greatly deplete the formation of protein corona. Therefore, we believed that less corona was formed on our nanoparticles, and gave less influence on the active targeting. To achieve even higher corona depletion and further enhance the active targeting capability of our nanoparticles, we plan to decorate their surface with zwitterionic coatings in the future, since the zwitterionic molecules have been recently reported as a promising method to deplete the protein corona and improve targeting efficiency of nanoparticles[31].

3.5 In vivo MRI

We further evaluated anti-EGFR-PEG-SPIO and PEGylated SPIO for MRI on nude rats bearing H460 lung tumor. T_2 SNR of H460 lung tumors after injection of the active targeting and non-targeting contrast agents are shown in Fig. 5 and Tab. S2. Thirty minutes after the injection of anti-EGFR-PEG-SPIO, the T_2 SNR in the lung tumor started to decrease. The T_2 SNR at the tumor region decreased more significantly at 4 hours post-injection of anti-EGFR-PEG-SPIO compared with the nontargeting group ($p<0.01$). This was likely caused by the higher accumulation of SPIO nanoparticles due to the active targeting effect of anti-EGFR-PEG-SPIO to the EGFR overexpressed H460 lung cancer xenograft. Prussian blue staining further demonstrated a higher SPIO deposition in tumor tissue in the anti-EGFR-PEG-SPIO group compared to the PEGylated SPIO group (Fig. 5c and d). This result was consistent with that shown in the MRI studies.

3.6 Biodistribution and clearance of anti-EGFR-PEG-SPIO and PEGylated SPIO NPs

Understanding the real biodistribution and clearance of anti-EGFR-PEG-SPIO is significant for its applications as a molecular probe for MR imaging. Fig. S2 and Tab. S3 illustrated the biodistribution of anti-EGFR-PEG-SPIO and PEGylated SPIO NPs in different organs such as heart, lung, liver, spleen, stomach, intestines, kidneys, blood, and tumor, at 24 h post-injection. This study shows that the iron concentration in liver and spleen was significantly higher than in heart, lung, stomach, and intestines at 24 h after injection. *In vivo* biodistribution patterns were similar between the targeting and nontargeting groups. The clearance mechanism of these nanoparticles were similar to that reported in previous studies, which was likely going through reticuloendothelial system (RES, mainly includes the organs like liver and spleen) and renal/urinary route [32–34].

3.7 In vivo synergistic MRgFUS lung tumor targeted ablation

Phase-difference maps of ablation (input power: 30–80 W; time: 20–25 seconds) and the temperature-time curve during ultrasound pulse (1.0 MHz) in left posterior thigh muscles of rats were shown in Fig. 6 (a and b) and Tab. 1. The sonication energy level used in the anti-EGFR-PEG-SPIO group (32 W) and PEGylated SPIO NPs group (54 W) were significantly lower than that in the positive control group (76 W) ($P<0.01$) (Fig. 6e and f). However, the peak temperatures in both anti-EGFR-PEG-SPIO and PEGylated SPIO NPs were very similar to that of the positive control group. Based on a previous report, SPIO containing microcapsules were able to enhance the ultrasonic wave absorption and energy deposition in tumor tissue [17]. Consistently, our results indicated that SPIO NPs had synergistic effect with the thermal therapy in MRgFUS system for tumor ablation. In this study, the energy of the targeting group was even lower than that of the nontargeting group (32 W vs 54 W, $P<0.01$) (Fig. 6 and Tab. 4). However, the achieved peak temperatures were roughly the same, demonstrating that anti-EGFR-PEG-SPIO could further enhance the efficiency for *in vivo* ultrasonic energy deposition. The increased energy deposition efficiency may be attributed to the higher accumulation of SPIO nanoparticles in the lung tumor sites with EGFR expression in the targeting group [35–37]. This result was consistent with that in *in vitro* and *in vivo* MR imaging studies (Fig. 4 and Fig. 5)**.** In the negative control group (low power, 54 W), the peak temperature was significantly lower than that of the PEGylated SPIO group with identical sonication power (54 W). The above finding indicated that: 1) SPIO NPs could improve the ultrasound energy deposition efficiency in tumor tissue at lower power and generate a synergistic effect in tumor thermal therapy; and 2) higher accumulation of SPIO NPs in the anti-EGFR-PEG-SPIO group through targeting EGFR overexpressing H460 lung cancer could further enhance the energy deposition efficiency in MRgFUS.

The entire MRgFUS ablation process was monitored by MRI. The T_2WI signal intensities of tumor increased significantly before and after MRgFUS therapy (Fig. 6g), indicating the degeneration and necrosis of the tumor tissue following ablation [38]. Enhanced axial T_1WI-weighted images after injection of gadolinium also showed an area of nonperfusion of the focal ablation (white) (Fig. 6g)

3.8 Post-treatment MR imaging

In the present study, we utilized a series of MRI sequences, such as T_2WI, DWI, and contrast-enhanced T_1WI imaging to guide the evaluation of therapeutic efficiency. Fig. 7(a–d) showed that T_2 signal intensities and ADC values increased gradually after ablation in a prolonged time course in the positive control (76 W), nontargeting (54 W), and targeting group (32 W). However, compared with the three previous groups, the negative control group (low power, 54 W) did not show similar results before and after ablation. Hypointense signals on T_2WI may be due to cystic degeneration or necrosis in tumors after treatment (Fig. 7a and e). A small black focal area of nonperfusion at series axial T_1WI indicated the lack of blood supply in the tumor after treatment (Fig. 7d), suggesting the absence or necrosis of tumor cells after MRgFUS ablation. These findings were consistent with that in previous results [39]. Tumor sizes in different treatment groups were measured at different time points after treatment. For the targeting group, MRI showed that the tumor tissue was

almost eliminated in two rats at 30 days (Fig. 7a and b and c). Post treatment, a significant decrease of tumor size in four other nude rats was observed, which was slightly smaller than those in the nontargeting and positive control group (Fig. 7f). Tumor size was significantly decreased in the positive control (76 W), nontargeting (54 W), and targeting group (32 W). In contrast, MRI showed tumor size increases in the negative control group (low power, 54 W)(Tab. S4).

After ablation, the expression of EGFR was absent in the necrotic region of three groups (positive control, nontargeting, and targeting), while the expression of EGFR was positive in the negative control group (low power) (Fig. 8a~d). The TUNEL staining results indicated that the percentage of apoptotic cells in the negative control (low power) group were much lower than those in the other three groups (Fig. 8e~h). The results from H&E staining showed more extensive necrotic areas in the positive control (76 W), nontargeting (54 W), and targeting group (32 W) than that in the negative control group (low power, 54 W) after MRgFUS ablation (Fig. 8i~l).

Discussion

The therapeutic efficacy of MRgFUS is relatively low for large volume tumor masses or deep lesions. With an increase of depth in tumor tissues, the ultrasound energy is attenuated exponentially, and therefore high ultrasound power must be employed to obtain the desired therapeutic efficacy. Such high acoustic energy could cause damage to normal surrounding tissues in the process of ultrasound, resulting in potential complications such as inadvertent injury to hollow viscera adjacent to the target tumor, nerve injury, and skin burns [38, 40–42]. Novel approaches that are able to obtain high therapeutic efficacy with low ultrasound power in MRgFUS therapy remains as a critical unmet clinical need.

To address the problem mentioned above, we proposed to develop a multifunctional MRgFUS synergistic agents for tumor treatment based on targeting nano-sized NPs, from which heat can be generated to specifically synergize tumor ablation accompanied with minimal complication to healthy tissues and surrounding organs. To the best of our knowledge, the present study evaluated the active targeting and nano-sized SPIO platform for the enhancement of imaging sensitivity and tumor-ablative efficacy in MRgFUS for the first time. The targeting and nano-sized SPIO platform has better targeting tropism to lung cancer *in vitro* and *in vivo* compared to SPIO NPs without medication by antibody. The design of targeting nano-sized NPs is particularly suitable for enhancing MRI sensitivity and the efficiency for *in vivo* ultrasonic energy deposition in MRgFUS, leading to fewer side effects.

Two main mechanisms may be involved to account for the synergistic effect caused by introduction of anti-EGFR-PEG-SPIO for MRgFUS ablation. Firstly, the anti-EGFR-PEG-SPIO has active targeting for lung cancer overexpressing EGFR, therefore, it could enhance the heat transfer rate in tissue in comparison to nontargeting NPs. Secondly, the introduction of SPIO NPs could change the acoustic microenvironment of the tumor tissue to improve ultrasound wave absorption and ultrasound energy deposition in tumor tissue [17]. The previous reported particles have very large sizes (587 nm & 885.6 nm) and their

accumulation in tumor was low [5, 17]. In contrast, our anti-EGFR-PEG-SPIO nanoparticles are nano-sized (40–50 nm), and their tumor accumulation could be further enhanced with active targeting mAb against EGFR. This platform could greatly improve the energy accumulation property in tumor regions and enhance targeted tissue hyperthermia by MRgFUS.

Conclusion

We have successfully developed an anti-EGFR mAb modified PEGylated SPIO nanoparticle as targeting MR imaging contrast agents and synergistic agents for MRgFUS ablation in lung carcinoma. These targeting nanoparticles significantly improved the MRI sensitivity for visualization of EGFR overexpressed lung cancer in a rat model. Furthermore, these nanoparticles are highly desirable for their ability to further enhance MRgFUS efficacy with lower energy levels, which may be able to the reduce side effects to surrounding normal tissues. Before and after tumor ablation, the therapeutic efficacy could be conveniently and noninvasively monitored by a series of novel MRI sequences, providing an attractive approach for treatment assessment. This targeting nano-theranostic platform shows great potential to improve the imaging sensitivity and treatment outcomes for clinical MRgFUS.

Supplementary Material

Refer to Web version on PubMed Central for supplementary material.

Acknowledgments

The authors would like to gratefully acknowledge the editorial assistance from Puiyan Ho and the technical support for MRgFUS studies from Na Tang. This work was financially supported by the National Nature Science of China (Grant NO. 81271384 and 81371623), NIH/NCI (R01CA199668) and NIH/NICHD (R01HD086195).

References

1. Cline HE, Hynynen K, Watkins RD, Adams WJ, Schenck JF, Ettinger RH, Freund WR, Vetro JP, Jolesz FA. Focused US system for MR imaging-guided tumor ablation. Radiology. 1995; 194:731–737. [PubMed: 7862971]
2. Gianfelice D, Khiat A, Amara M, Belblidia A, Boulanger Y. MR imaging–guided focused us ablation of breast cancer: Histopathologic assessment of effectiveness—initial experience 1. Radiology. 2003; 227:849–855. [PubMed: 12714680]
3. Jolesz FA, Hynynen K. Magnetic resonance image-guided focused ultrasound surgery. Cancer journal (Sudbury, Mass). 2001; 8:S100–12.
4. Ishihara Y, Calderon A, Watanabe H, Okamoto K, Suzuki Y, Kuroda K, Suzuki Y. A precise and fast temperature mapping using water proton chemical shift. Magnetic Resonance in Medicine. 1995; 34:814–823. [PubMed: 8598808]
5. Sun Y, Zheng Y, Li P, Wang D, Niu C, Gong Y, Huang R, Wang Z, Wang Z, Ran H. Evaluation of superparamagnetic iron oxide-polymer composite microcapsules for magnetic resonance-guided high-intensity focused ultrasound cancer surgery. BMC cancer. 2014; 14:1. [PubMed: 24383403]
6. Chen Y, Chen H, Sun Y, Zheng Y, Zeng D, Li F, Zhang S, Wang X, Zhang K, Ma M. Multifunctional Mesoporous Composite Nanocapsules for Highly Efficient MRI-Guided High-Intensity Focused Ultrasound Cancer Surgery. Angewandte Chemie International Edition. 2011; 50:12505–12509. [PubMed: 22076783]

7. Foldager CB, Pedersen M, Ringgaard S, Bünger C, Lind M. Chondrocyte gene expression is affected by very small iron oxide particles-labeling in long-term in vitro MRI tracking. Journal of Magnetic Resonance Imaging. 2011; 33:724–730. [PubMed: 21563258]
8. Protti A, Dong X, Andia ME, Yu B, Dokukina K, Chaubey S, Phinikaridou A, Vizcay-Barrena G, Taupitz M, Botnar RM. Assessment of inflammation with a very small iron-oxide particle in a murine model of reperfused myocardial infarction. Journal of Magnetic Resonance Imaging. 2014; 39:598–608. [PubMed: 24006053]
9. Wagner M, Wagner S, Schnorr J, Schellenberger E, Kivelitz D, Krug L, Dewey M, Laule M, Hamm B, Taupitz M. Coronary MR angiography using citrate-coated very small superparamagnetic iron oxide particles as blood-pool contrast agent: Initial experience in humans. Journal of Magnetic Resonance Imaging. 2011; 34:816–823. [PubMed: 21769977]
10. Zhou Z, Sun Y, Shen J, Wei J, Yu C, Kong B, Liu W, Yang H, Yang S, Wang W. Iron/iron oxide core/shell nanoparticles for magnetic targeting MRI and near-infrared photothermal therapy. Biomaterials. 2014; 35:7470–7478. [PubMed: 24881997]
11. Fu G, Liu W, Li Y, Jin Y, Jiang L, Liang X, Feng S, Dai Z. Magnetic Prussian blue nanoparticles for targeted photothermal therapy under magnetic resonance imaging guidance. Bioconjugate chemistry. 2014; 25:1655–1663. [PubMed: 25109612]
12. Yang F, Li Y, Chen Z, Zhang Y, Wu J, Gu N. Superparamagnetic iron oxide nanoparticle-embedded encapsulated microbubbles as dual contrast agents of magnetic resonance and ultrasound imaging. Biomaterials. 2009; 30:3882–3890. [PubMed: 19395082]
13. Lee J-H, Jang J-t, Choi J-s, Moon SH, Noh S-h, Kim J-w, Kim J-G, Kim I-S, Park KI, Cheon J. Exchange-coupled magnetic nanoparticles for efficient heat induction. Nature nanotechnology. 2011; 6:418–422.
14. Shuai X, Ai H, Nasongkla N, Kim S, Gao J. Micellar carriers based on block copolymers of poly (ε-caprolactone) and poly (ethylene glycol) for doxorubicin delivery. Journal of Controlled Release. 2004; 98:415–426. [PubMed: 15312997]
15. Mouli SK, Tyler P, McDevitt JL, Eifler AC, Guo Y, Nicolai J, Lewandowski RJ, Li W, Procissi D, Ryu RK. Image-guided local delivery strategies enhance therapeutic nanoparticle uptake in solid tumors. ACS nano. 2013; 7:7724–7733. [PubMed: 23952712]
16. Gordon AC, Lewandowski RJ, Salem R, Day DE, Omary RA, Larson AC. Localized Hyperthermia with Iron Oxide–Doped Yttrium Microparticles: Steps toward Image-Guided Thermoradiotherapy in Liver Cancer. Journal of Vascular and Interventional Radiology. 2014; 25:397–404. [PubMed: 24315666]
17. Sun Y, Zheng Y, Ran H, Zhou Y, Shen H, Chen Y, Chen H, Krupka TM, Li A, Li P. Superparamagnetic PLGA-iron oxide microcapsules for dual-modality US/MR imaging and high intensity focused US breast cancer ablation. Biomaterials. 2012; 33:5854–5864. [PubMed: 22617321]
18. Li J, Hu Y, Yang J, Wei P, Sun W, Shen M, Zhang G, Shi X. Hyaluronic acid-modified Fe_3O_4@ Au core/shell nanostars for multimodal imaging and photothermal therapy of tumors. Biomaterials. 2015; 38:10–21. [PubMed: 25457979]
19. Guo Y, Zhang Z, Kim DH, Li W, Nicolai J, Procissi D, Huan Y, Han G, Omary RA, Larson AC. Photothermal ablation of pancreatic cancer cells with hybrid iron-oxide core gold-shell nanoparticles. International journal of nanomedicine. 2013; 8:3437. [PubMed: 24039426]
20. Wu H, Wang H, Liao H, Lv Y, Song X, Ma X, Tan M. Multifunctional Nanostructures for Tumor-Targeted Molecular Imaging and Photodynamic Therapy. Advanced healthcare materials. 2016; 5:311–318. [PubMed: 26626703]
21. Scaltriti M, Baselga J. The epidermal growth factor receptor pathway: a model for targeted therapy. Clinical Cancer Research. 2006; 12:5268–5272. [PubMed: 17000658]
22. Garousi J, Andersson KG, Mitran B, Pichl M-L, Ståhl S, Orlova A, Löfblom J, Tolmachev V. PET imaging of epidermal growth factor receptor expression in tumours using 89Zr-labelled ZEGFR: 2377 affibody molecules. International journal of oncology. 2016; 48:1325–1332. [PubMed: 26847636]

23. Jia Q, Zeng J, Qiao R, Jing L, Peng L, Gu F, Gao M. Gelification: an effective measure for achieving differently sized biocompatible Fe3O4 nanocrystals through a single preparation recipe. Journal of the American Chemical Society. 2011; 133:19512–19523. [PubMed: 22029389]
24. Liu S, Jia B, Qiao R, Yang Z, Yu Z, Liu Z, Liu K, Shi J, Ouyang H, Wang F. A novel type of dual-modality molecular probe for MR and nuclear imaging of tumor: preparation, characterization and in vivo application. Molecular pharmaceutics. 2009; 6:1074–1082. [PubMed: 19527074]
25. Zhang Z, Hu Y, Yang J, Xu Y, Zhang C, Wang Z, Shi X, Zhang G. Facile Synthesis of Folic Acid-Modified Iron Oxide Nanoparticles for Targeted MR Imaging in Pulmonary Tumor Xenografts. Molecular Imaging and Biology. 2015:1–10. [PubMed: 25238997]
26. Wang Z, Zhu J, Chen Y, Geng K, Qian N, Cheng L, Lu Z, Pan Y, Guo L, Li Y. Folic acid modified superparamagnetic iron oxide nanocomposites for targeted hepatic carcinoma MR imaging. RSC Advances. 2014; 4:7483–7490.
27. Patterson A. The Scherrer formula for X-ray particle size determination. Physical review. 1939; 56:978.
28. Mirshafiee V, Mahmoudi M, Lou K, Cheng J, Kraft ML. Protein corona significantly reduces active targeting yield. Chemical communications. 2013; 49:2557–2559. [PubMed: 23423192]
29. Schöttler S, Becker G, Winzen S, Steinbach T, Mohr K, Landfester K, Mailänder V, Wurm FR. Protein adsorption is required for stealth effect of poly (ethylene glycol)-and poly (phosphoester)-coated nanocarriers. Nature nanotechnology. 2016; 11:372–377.
30. Liu S, Han Y, Qiao R, Zeng J, Jia Q, Wang Y, Gao M. Investigations on the interactions between plasma proteins and magnetic iron oxide nanoparticles with different surface modifications. The Journal of Physical Chemistry C. 2010; 114:21270–21276.
31. Mahmoudi M, Bertrand N, Zope H, Farokhzad OC. Emerging understanding of the protein corona at the nano-bio interfaces. Nano Today. 2016; 11:817–832.
32. Duan X, Li Y. Physicochemical characteristics of nanoparticles affect circulation, biodistribution, cellular internalization, and trafficking. Small. 2013; 9:1521–1532. [PubMed: 23019091]
33. Janát-Amsbury M, Ray A, Peterson C, Ghandehari H. Geometry and surface characteristics of gold nanoparticles influence their biodistribution and uptake by macrophages. European Journal of Pharmaceutics and Biopharmaceutics. 2011; 77:417–423. [PubMed: 21093587]
34. Wang H, Zheng L, Peng C, Shen M, Shi X, Zhang G. Folic acid-modified dendrimer-entrapped gold nanoparticles as nanoprobes for targeted CT imaging of human lung adencarcinoma. Biomaterials. 2013; 34:470–480. [PubMed: 23088841]
35. Kopelman D, Inbar Y, Hanannel A, Freundlich D, Vitek S, Schmidt R, Sokolov A, Hatoum OA, Rabinovici J. Magnetic resonance-guided focused ultrasound surgery using an enhanced sonication technique in a pig muscle model. European journal of radiology. 2006; 59:190–197. [PubMed: 16765006]
36. Liao C, Sun Q, Liang B, Shen J, Shuai X. Targeting EGFR-overexpressing tumor cells using Cetuximab-immunomicelles loaded with doxorubicin and superparamagnetic iron oxide. European journal of radiology. 2011; 80:699–705. [PubMed: 20810233]
37. Chung TH, Hsiao JK, Hsu SC, Yao M, Chen YC, Wang SW, Kuo MYP, Yang CS, Huang DM. Iron oxide nanoparticle-induced epidermal growth factor receptor expression in human stem cells for tumor therapy. ACS nano. 2011; 5:9807–9816. [PubMed: 22053840]
38. Funaki K, Fukunishi H, Funaki T, Sawada K, Kaji Y, Maruo T. Magnetic resonance-guided focused ultrasound surgery for uterine fibroids: relationship between the therapeutic effects and signal intensity of preexisting T2-weighted magnetic resonance images. American journal of obstetrics and gynecology. 2007; 196:184.e1–184.e6. [PubMed: 17306674]
39. Pore N, Jiang Z, Gupta A, Cerniglia G, Kao GD, Maity A. EGFR tyrosine kinase inhibitors decrease VEGF expression by both hypoxia-inducible factor (HIF)-1–independent and HIF-1–dependent mechanisms. Cancer research. 2006; 66:3197–3204. [PubMed: 16540671]
40. Li JJ, Xu GL, Gu MF, Luo GY, Rong Z, Wu PH, Xia JC. Complications of high intensity focused ultrasound in patients with recurrent and metastatic abdominal tumors. World journal of gastroenterology. 2007; 13:2747. [PubMed: 17569147]

41. Li YY, Sha WH, Zhou YJ, Nie YQ. Short and long term efficacy of high intensity focused ultrasound therapy for advanced hepatocellular carcinoma. Journal of gastroenterology and hepatology. 2007; 22:2148–2154. [PubMed: 18031373]

42. Ma M, Zhang Y, Gong H, Li F, Gu N. Silica-coated magnetite nanoparticles labeled by nimotuzumab, a humanised monoclonal antibody to epidermal growth factor receptor: Preparations, specific targeting and bioimaging. Journal of nanoscience and nanotechnology. 2013; 13:6541–6545. [PubMed: 24245112]

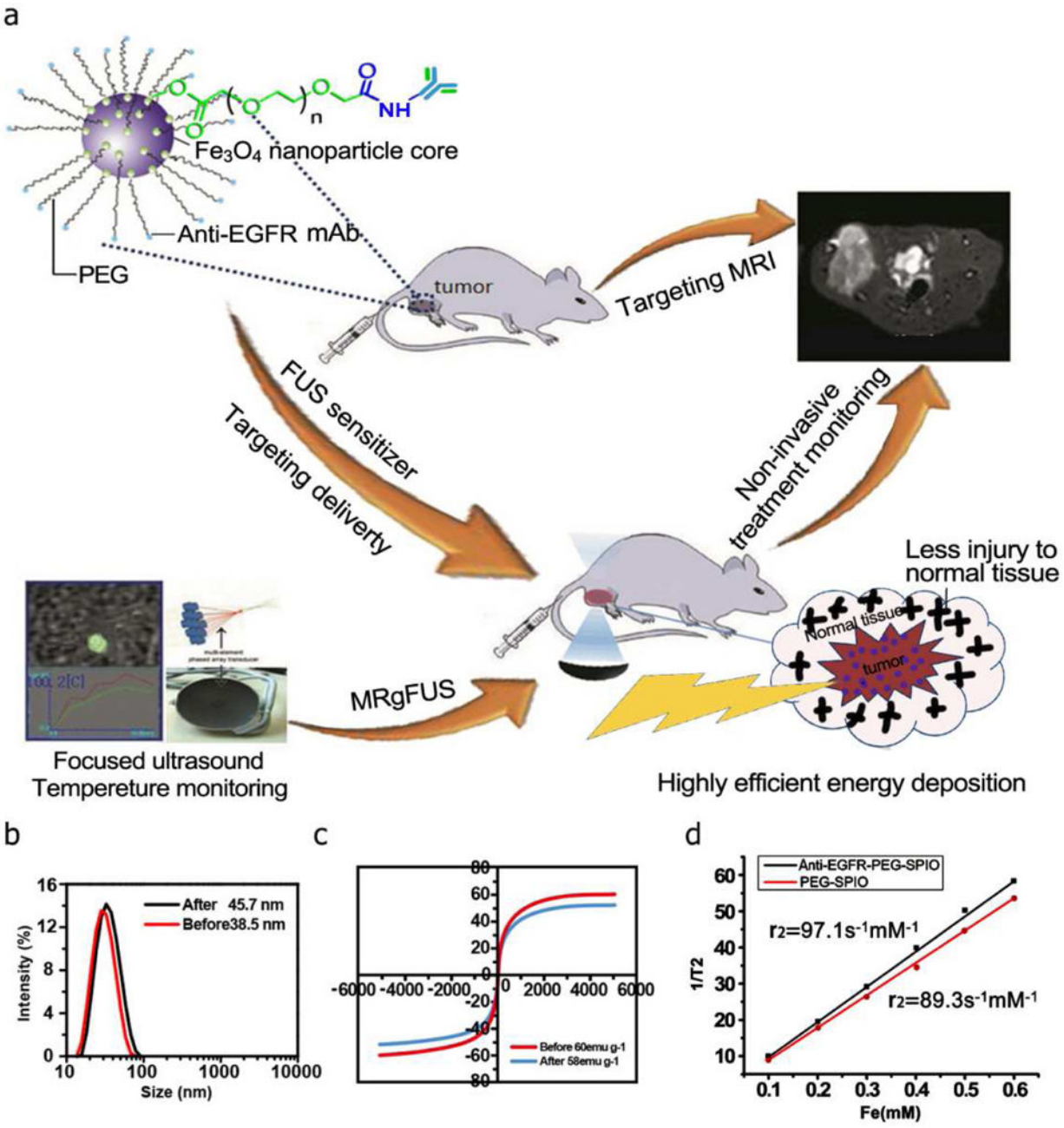

Fig. 1.

(a) Scheme of the formulation process for anti-EGFR-PEG-SPIO NPs and their applications in MRgFUS. (b) The DLS results showed that diameter was about 38.5 nm for PEGylated SPIO and 45.7 nm for anti-EGFR-PEG-SPIO. (c) The hysteresis loop of anti-EGFR-PEG-SPIO and PEGylated SPIO at 298 k, magnetization (M) value was 58 emu g^{-1}. (d) T_2 relativity values were 97.1 $mM^{-1}s^{-1}$ for anti-EGFR-PEG-SPIO and 89.3 $mM^{-1}s^{-1}$ for PEGylated SPIO.

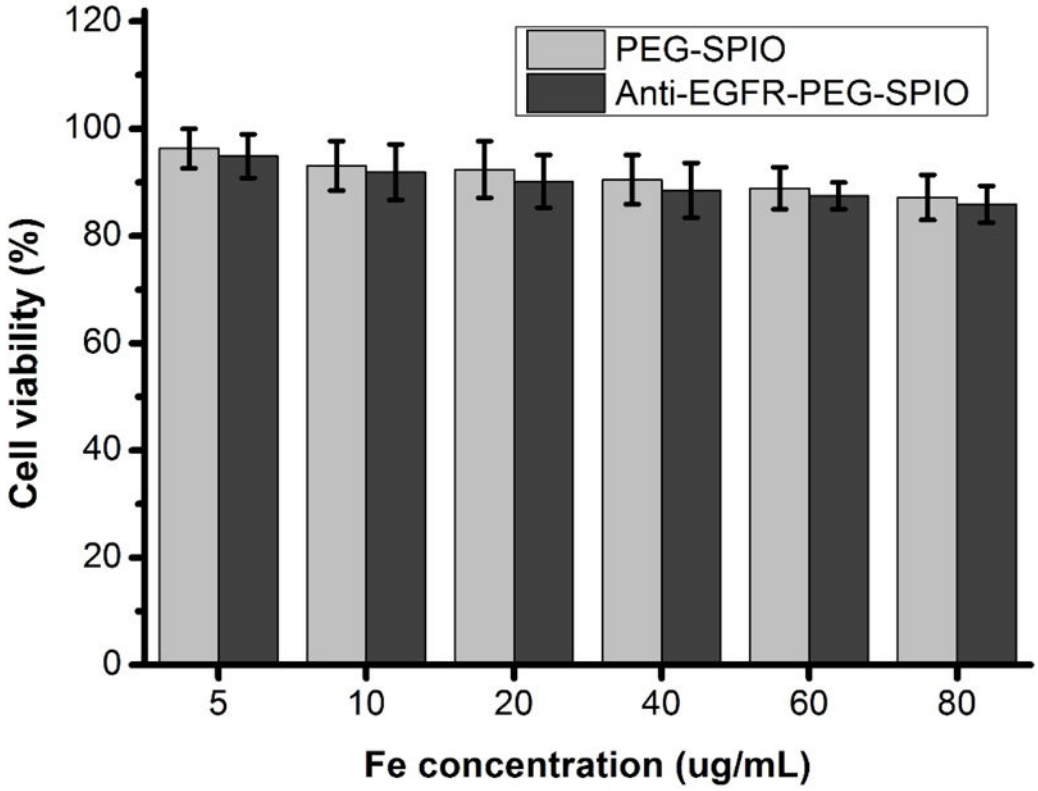

Fig. 2.

H460 cells viability after incubation with anti-EGFR-PEG-SPIO and PEGylated SPIO (Fe concentration: 10–80 μg/mL) for 24 hours by MTT assay.

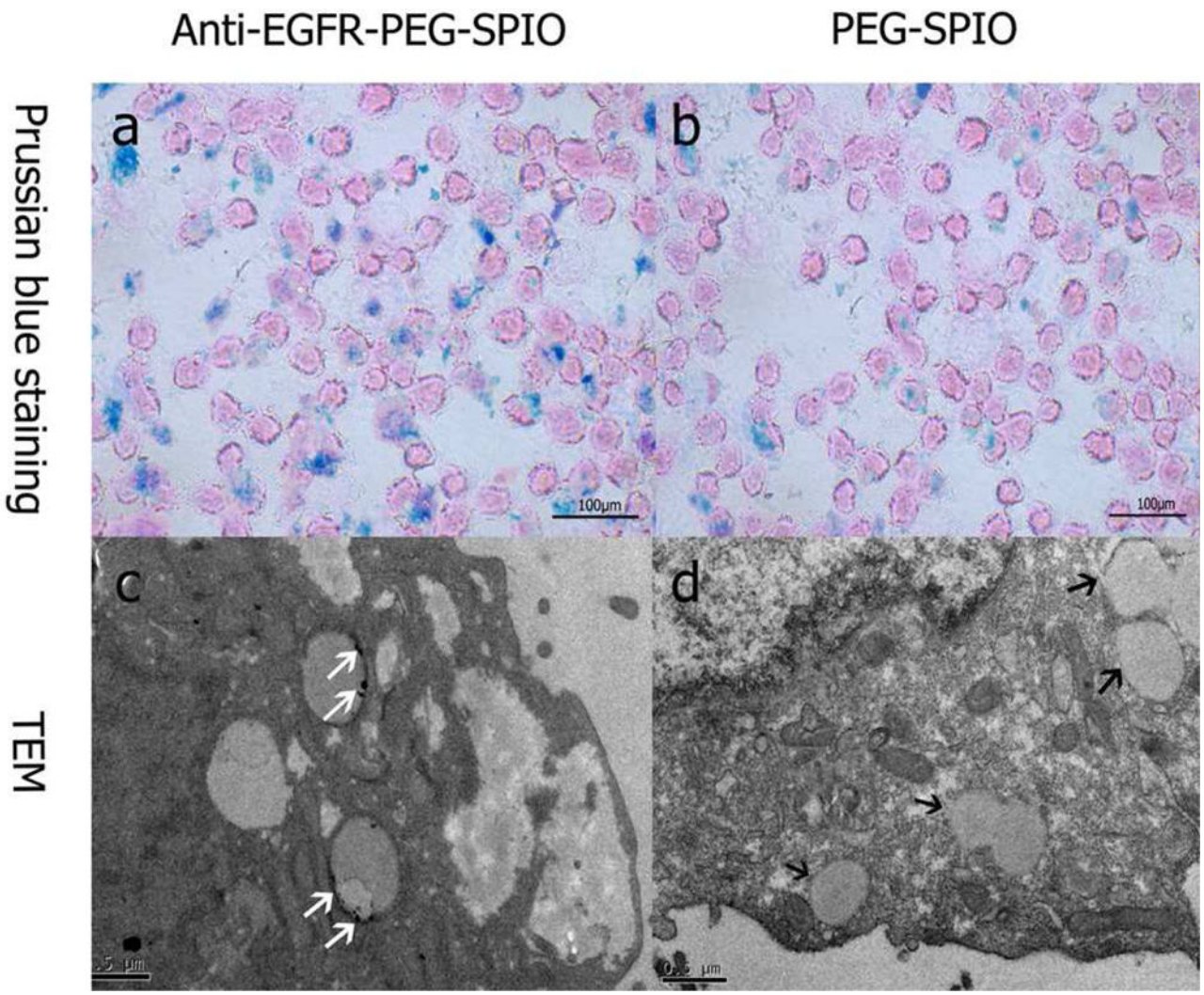

Fig. 3.

Prussian blue staining images (×200) of H460 cells (1×10^6) after 2 h incubation with anti-EGFR-PEG-SPIO (a) and PEGylated SPIO (b). TEM images of H460 cells after 12 h incubation with anti-EGFR-PEG-SPIO (c) and PEGylated SPIO (d). The white arrow shows iron particles located at the endosomes. The black arrow shows no obvious iron particles were observed in the endosomes.

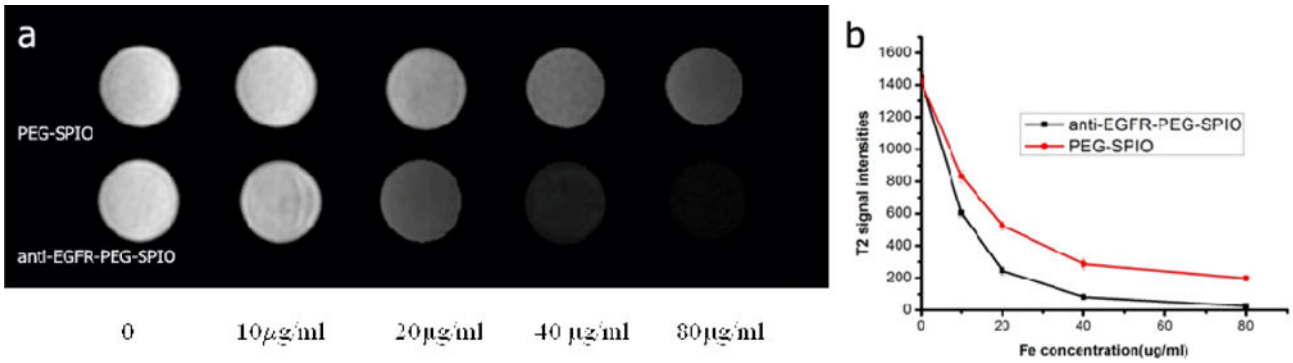

Fig. 4.

In vitro MR images analysis of H460 cells treated with PEGylated SPIO and anti-EGFR-PEG-SPIO at different iron concentration for 2 h (a). A low T_2 signal intensity negatively correlates with iron concentration. T_2 signal intensities reduced significantly when the iron concentration is increased to 20 μg/mL (a & b). The unobvious change of T_2 signal intensities (a & b).

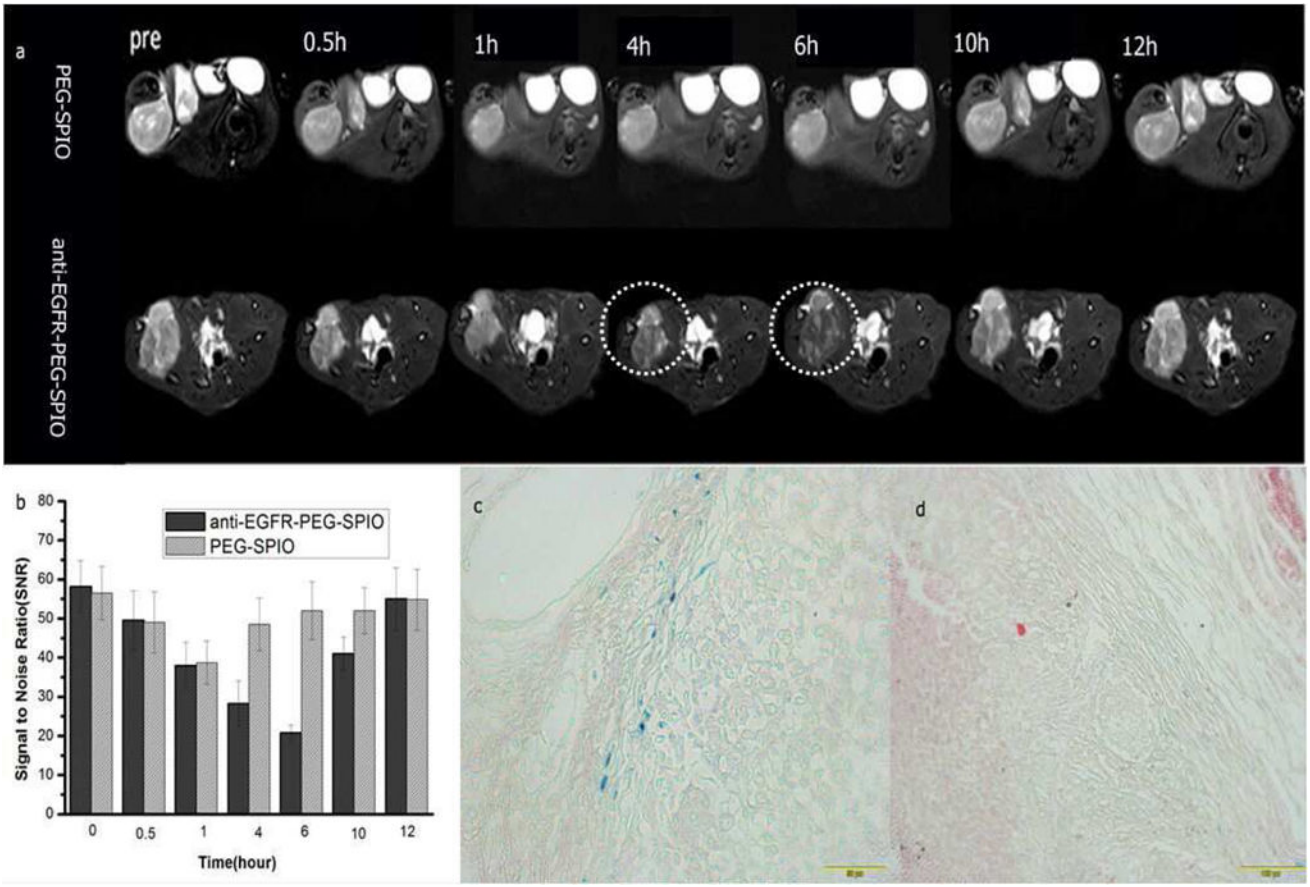

Fig. 5.

T_2WI MRI images (a) and SNR (b) of tumor after injection of 0.1 mL targeting and nontargeting contrasting agents at different time points (0.5, 1, 4, 6, 10, 12 h). The mean T_2-weighted signal intensities were measured for each tumor. The relative SNR was calculated. Prussian blue staining of tumor tissues after 6 h injection of (c) anti-EGFR-PEG-SPIO and (d) PEGylated SPIO.

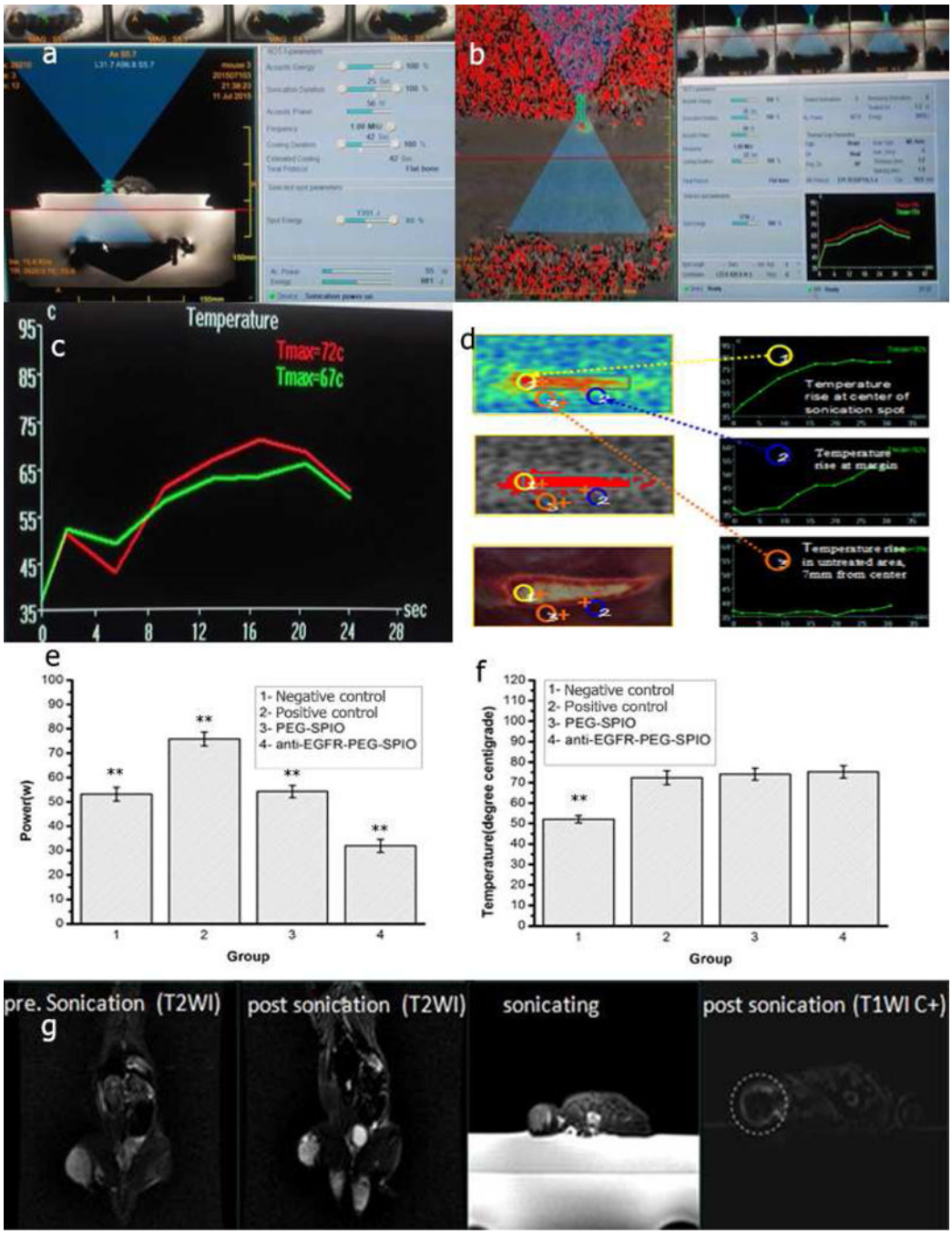

Fig. 6.

(a) Sonication process images. Treatment planning software on the MRgFUS workstation. In total, 5 sonications are needed to measure the circumference of this tumor. (b) Tissue temperature mapping during MRgFUS ablation. (c) Real-time temperature change in MRgFUS ablation monitored by MRI. (d) Schematic illustration of therapeutic temperature map in tumor center and margin. Sonication energy (e) and therapeutic peak temperature (f) of negative control (low power, 54 W), control (76 W), PEG-SPIO (54 W), and anti-EGFR-PEG-SPIO (32 W) at 4 h post-injection of SPIO nanoparticles. (g) Anti-EGFR-PEG-SPIO

group: Coronal T_2WI image signal intensity of tumor before treatment and after treatment. The coronal T_2WI signal intensities of tumor increased significantly after therapy compared to before therapy (Fig. 6g). Enhanced axial T_1WI-weighted images after injection of Gd-DTPA. Axial contrast-enhance T_1WI subtraction images after injection of Gd-DTPA showed a small focal area of nonperfusion.

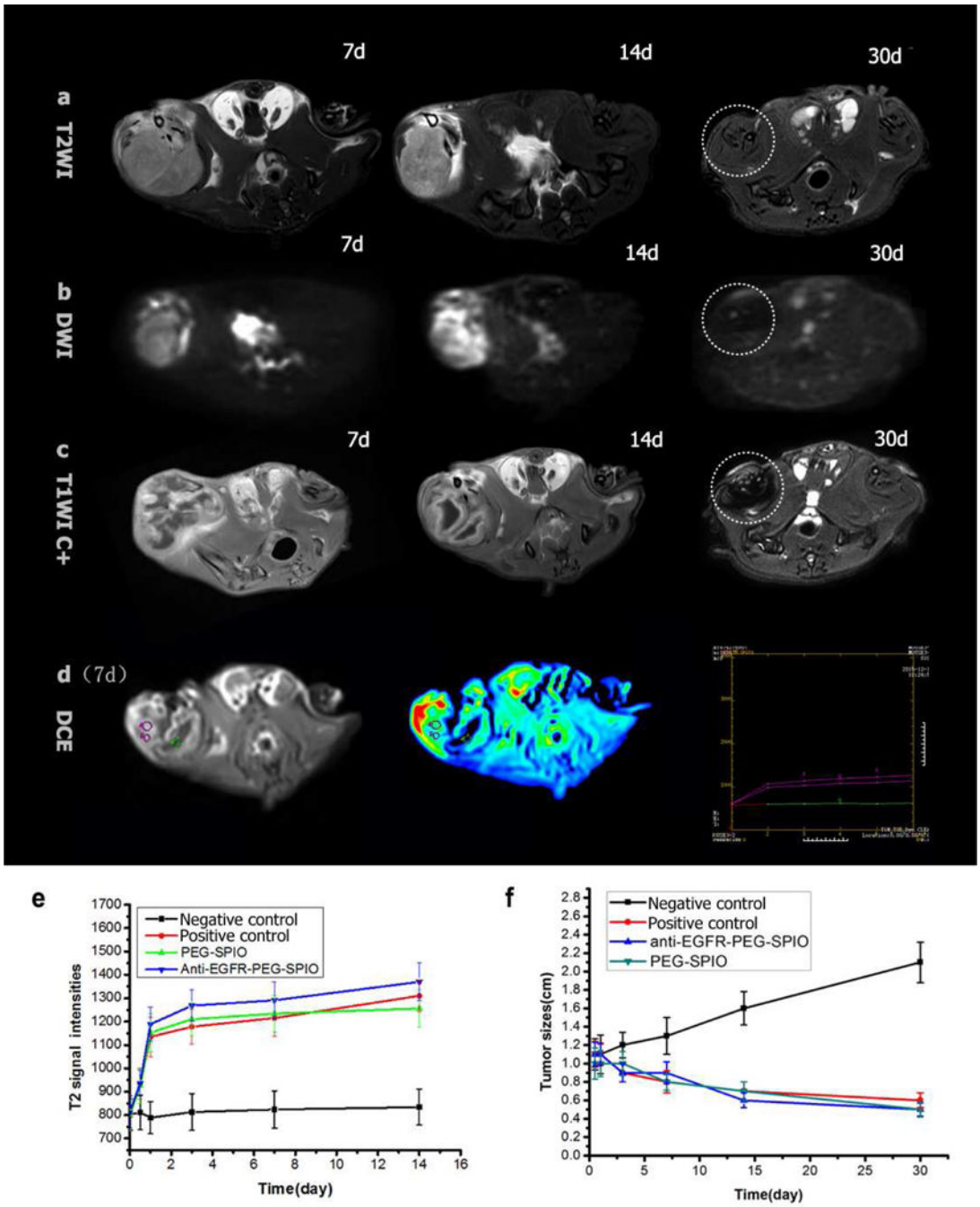

Fig. 7.

Anti-EGFR-PEG-SPIO group: (a and b) axial T_2WI and DWI images at 7, 14, 30 d after MRgFUS ablation, T_2 signal intensities and ADC values increased gradually after ablation. T_2WI and DWI images show complete tumor elimination at 30 days after MRgFUS treatment. (c) Axial contrast-enhance T_1WI images show small focal area of nonperfusion (black unenhanced area) at different time points after MRgFUS ablation (7, 14, 30 d). (e and f) T_2WI images and tumor size change images before and after MRgFUS ablation of negative control (low power), positive control, PEGylated SPIO, and anti-EGFR-PEG-SPIO.

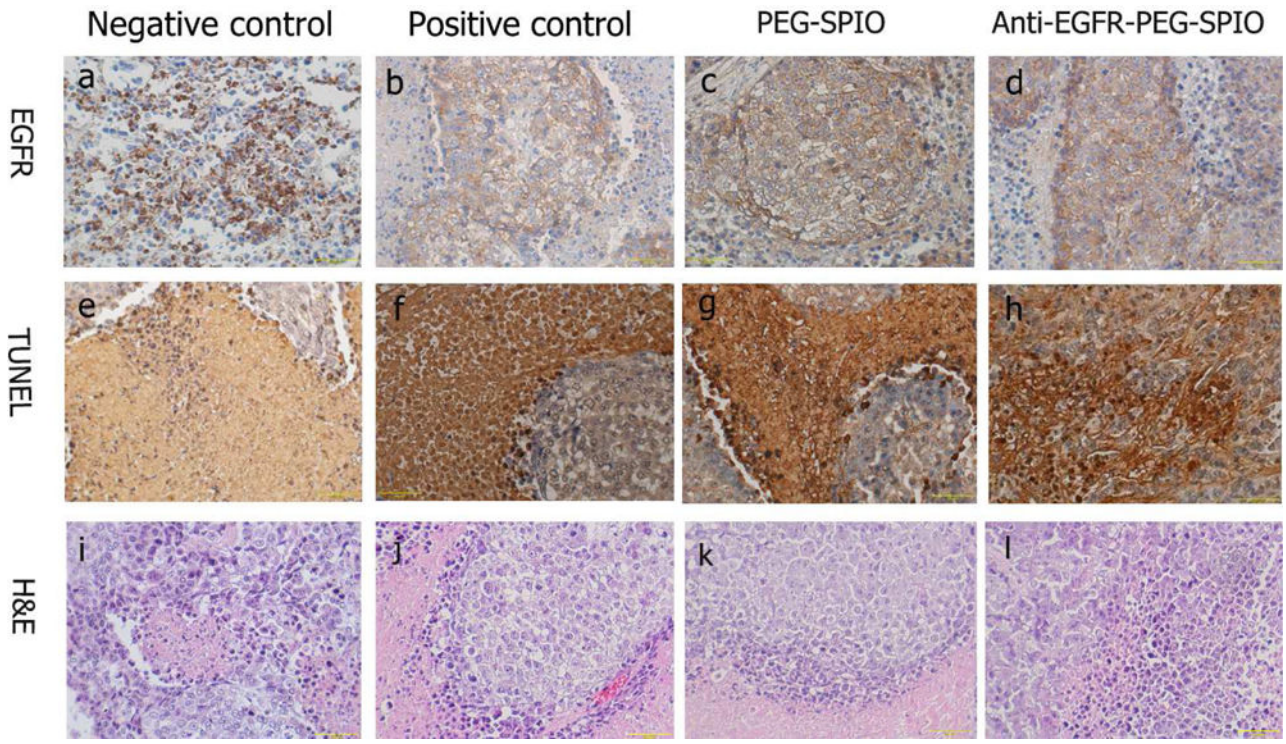

Fig. 8.

The expression of EGFR in tumor tissue after MRgFUS ablation by immunohistochemistry. The nucleus appeared brown (a) in EGFR-positive cells, blue in negative cells (b and c and d). TUNEL staining images showed that the percentage of apoptotic cells in (e) were much lower than those in (f and j and h). (i~l) H&E staining of tumor tissue in negative control (low power), positive control, PEGylated SPIO and anti-EGFR-PEG-SPIO group.

Tab. 1

Power, treatment time, and peak temperature of the four groups

Groups/parameter	Negative control	Positive control	PEG-SPIO	Anti-EGFR-PEG-SPIO
Power(W)	53.8±2.8	75.8 ±2.9	54.3 ±2.5	32.0±2.7
Treatment time(s)	24.2±1.1	23.2±1.2	24.0±1.2	24.2±1.0
Temperature(°C)	52.1±1.8	72.4±3.4	74.1±2.9	75.2±3.0

Power, treatment time, and peak temperature are presented as mean±standard deviation, SD